Rapid and sensitive XAFS using a tunable X-ray undulator at BL10XU of SPring-8

Hiroyuki Oyanagi,[a]* Masashi Ishii,[b] Chul-Ho Lee,[a] Naurang L. Saini,[c] Yuji Kuwahara,[d] Akira Saito,[d] Yasuo Izumi[e] and Hideki Hashimoto[f]

[a]*Electrotechnical Laboratory, 1-1-4 Umezono, Tsukuba 305-8568, Japan,* [b]*JASRI, Kamigori, Ako-gun, Hyogo 678-12, Japan,* [c]*Universita di Roma 'La Sapienza', Dipartimento di Fisica, 00185 Roma, Italy,* [d]*Osaka University, 2-1 Yamadaoka, Suita, Osaka 565-0871, Japan,* [e]*Tokyo Institute of Technology, 4259 Nagatsuta, Midori-ku, Yokohama 226-8502, Japan, and* [f]*TORAY Research Center, 337 Sonoyama, Otsu-shi 520-8567, Japan.* E-mail: oyanagi@etl.go.jp

The design and performance of the high-brilliance XAFS facility at BL10XU of SPring-8, aimed at rapid and sensitive measurement of X-ray absorption fine structure (XAFS), is reported. Both undulator gap and double-crystal monochromator have been successfully controlled covering a wide energy range (5–30 keV). A versatile goniometer system, consisting of two independent high-precision goniometers, is capable of polarized XAFS in fluorescence mode and surface-sensitive experiments using a grazing-incidence geometry. By sharing major components, *i.e.* a monolithic Ge 100-pixel array detector and a closed-cycle He cryostat, both polarized XAFS and X-ray standing wave (XSW) experiments can be performed at low temperature (15–300 K). The performance of the spectrometer has been evaluated by recording XAFS spectra in transmission mode.

1. Introduction

Tunable X-ray undulators inserted into straight sections of ultralow-emittance (<10 nm rad) storage rings have opened up new opportunities for local structure studies beyond the limitations in concentration and/or measurement time. Rapid and sensitive X-ray absorption fine structure (XAFS) (Chance, 1994) is particularly useful for *in situ* studies where the number of excited species of atom is strictly limited. For example, it has been demonstrated that pump-and-probe XAFS (Oyanagi *et al.*, 1998) can provide a 'snapshot' or 'frozen' radial distribution, serving as a probe of the local lattice distortion, relaxation and bond alternation as a result of optical excitation (Kolobov *et al.*, 1997). The observation that the time-averaged and spatially averaged coordination number of chalcogen atoms in chalcogenide glasses such as Se or As_2Se_3 increases during illumination at low temperature showed that the dominant photo-induced defect state is a pair of neutral C^0_3 states (C^0_3–C^0_3) and not a charged defect pair such as C^+_3–C^-_1 which would give the same average coordination number as that of the original state (Kolobov *et al.*, 1997).

Rapid and sensitive XAFS based on fluorescence detection and a tunable undulator, discussed in terms of mere feasibility in the early 1990s (Oyanagi, 1993), is now becoming a routine tool (Rogalev *et al.*, 1998). In this paper

we turn our attention to efforts to combine a tunable undulator and a high-efficiency X-ray detector. We have designed and built a high-brilliance XAFS apparatus at one of the undulator beamlines, BL10XU, of SPring-8. A novel 100-pixel array detector (PAD) has been recently developed as a high-throughput X-ray detector (Oyanagi, 1999). By computer control of the undulator deflection parameter and a double-crystal monochromator, a continuous scan over a wide energy range (5–30 keV) with a high energy resolution ($\Delta E/E < 2 \times 10^{-4}$) has been achieved. Another feature of the spectrometer is a versatile goniometer system which allows various polarization geometries or sample orientations.

Fluorescence-detected polarized XAFS experiments for cuprate superconductors demonstrated that the local structure of the conducting (CuO_2) plane is microscopically inhomogeneous, *i.e.* distorted 'localized' and undistorted 'itinerant' domains form charge and lattice stripes (Bianconi *et al.*, 1996). In order to investigate the role of stripes in high-T_c superconductivity, however, more efficient measurements of polarized XAFS are required. More recently, a large local lattice distortion (Jahn–Teller distortion) in manganites was found upon the charge and orbital ordering (Argyriou *et al.*, 1996). Much attention has been paid to the microscopic origin of colossal magnetoresistance (CMR) which arises from a competition between the lattice distortions and charge dynamics for the

charge carriers. Polarized XAFS studies provide important information on the symmetry and magnitude of local lattice distortions in cuprates and manganites. In order to study the temperature dependence of anisotropic radial distributions, a high-precision goniometer system with a cryostat is needed. In this paper we report a newly designed goniometer system which provides all the requirements described above.

2. Undulator and beamline optics

We briefly describe the optics of BL10XU at SPring-8 in the following. Major optical components are a rotated-inclined double-crystal monochromator (Ishikawa, 1995) and a
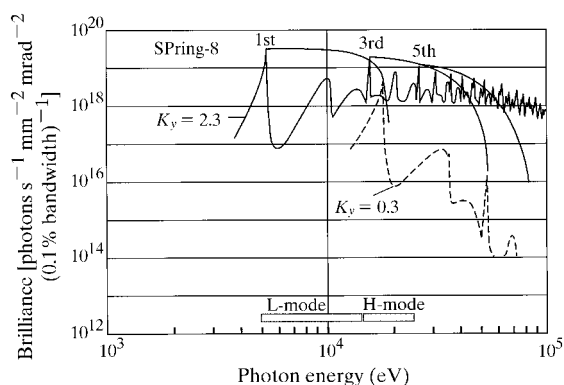

Figure 1
On-axis brilliance of an in-vacuum-type undulator for BL10XU at SPring-8 with a beam current of 100 mA (Kitamura, 1994). Two spectra with deflection parameter values ($K_y = 0.3, 2.3$) are shown on a logarithmic scale.

double flat mirror (Uruga *et al.*, 1995). In Fig. 1, undulator brilliance spectra for a standard in-vacuum-type undulator (U032V) (Kitamura, 1994) with deflection parameters $K_y = 0.3$ and 2.3 are shown. K_y depends on the magnetic field of the magnet array which is given as a function of the magnet gap. On varying the undulator gap from 9.6 mm to 22 mm a wide energy range (5–30 keV) is covered, using the first and third higher harmonics (L mode, $n = 1$; H mode, $n = 3$). On decreasing K_y, the peak positions shift to higher energy, giving smooth envelope functions shown by the solid line. Since a typical energy range of a routine extended X-ray absorption fine structure (EXAFS) scan is ~1 keV, both monochromator and undulator should be controlled during a scan. Higher harmonics and background radiation are minimized by a double flat mirror with a variable critical energy.

In Fig. 1 the on-axis brilliance of the in-vacuum undulator at SPring-8 is plotted as a function of photon energy, assuming a beam current of 100 mA. The brilliance, which is greater than that of a multipole wiggler at second-generation storage rings by more than four orders of magnitude, is a clear advantage of an undulator providing a high photon flux for a single-crystal (typically 1 mm in dimension) experiment or a grazing-incidence geometry (~100 µm aperture). Note that owing to the highest energy of a storage ring (8 GeV) among the third-generation facilities the envelope functions have the most flat intensity distribution over a wide energy range. The principle of a tuning undulator is briefly described in the following. First, the whole energy range was split into two regions, *i.e.* L-mode and H-mode. In the lower energy range (5–15 keV) the fundamental radiation ($n = 1$) is used while in the
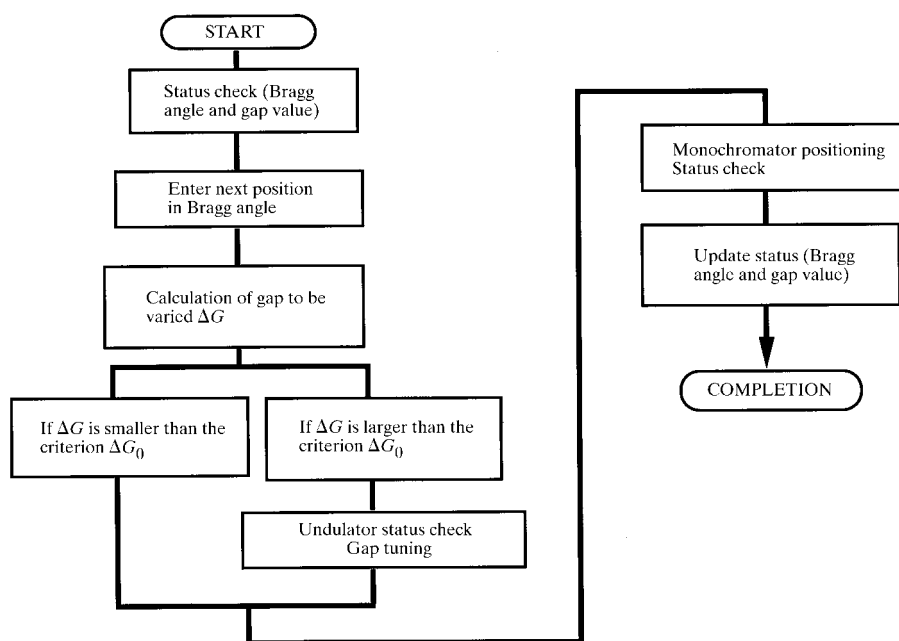

Figure 2
Flow chart of undulator gap control. Prior to monochromator control, a gap to be varied in mm (ΔG) is evaluated. When ΔG exceeds the user-programmable allowance value, ΔG_0 (10–30%), the undulator gap is tuned.

higher energy range (15–30 keV) the third higher harmonic radiation ($n = 3$) is tuned. Since the speed of positioning a magnet array for an in-vacuum-type undulator was mechanically limited (1 mm min^{-1}), the undulator gap is tuned when the intensity is reduced beyond a user-programmable allowance parameter ΔG_0 (10–30%). In the lower energy range a flat double mirror is inserted which can vary the cut-off energy so that the higher harmonics content is minimized.

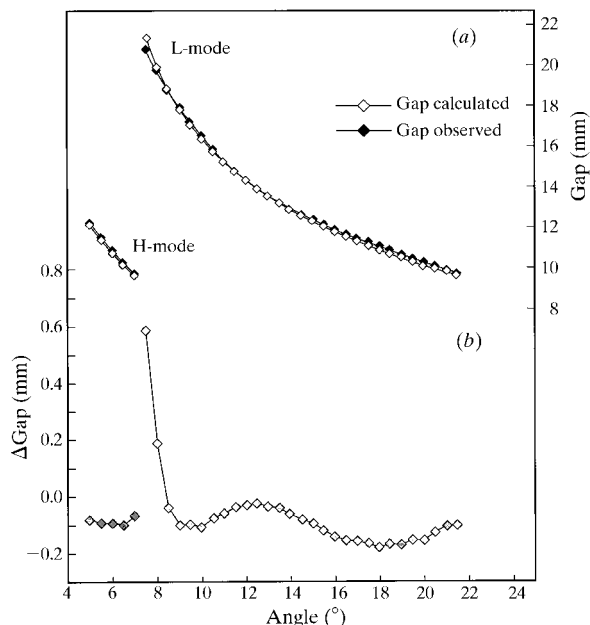There could be several approaches for undulator gap control. Rogalev *et al.* (1998) scanned the undulator whenever the gap value to be changed, ΔG, exceeded the minimum step of gap control, ΔG_{min}. The advantage of this method is that one can obtain the most smooth intensity distribution, tracing the envelope functions of peak intensity. However, this would take a long time since the gap is most frequently tuned. In the present case another approach, *i.e.* a variable tuning condition, has been adopted because of a mechanical limitation in the speed of the magnet array. As illustrated by the schematic flow chart shown in Fig. 2, ΔG (variation of gap value) is calculated each time the monochromator angle θ_B is requested to change. The undulator gap is tuned when the stored accumulated value exceeds the allowance parameter ΔG_0 calculated from the width of the undulator peak as a function of energy (Sasaki, 1994). In Fig. 3(*a*), calculated and observed gap values giving a maximum intensity are compared. The empirical gap values giving the maximum intensity were fitted by a quadratic polynomial $F(\theta_B)$ where θ_B denotes the Bragg angle of the monochromator. Fig. 3(*b*) shows the deviations of gap values (error) from the calculated ones as a function of θ_B. The calculated full width at half-maximum (FWHM) values for $n = 1$ and $n = 3$ (Sasaki, 1994) were fitted by a simple formula: $G(\theta_B) = \alpha\theta_B{}^\beta$, where α and β are free parameters and the magnitude of allowance parameter was obtained from $G(\theta_B)$ after the coefficient α was normalized. Using $F(\theta_B)$ and $G(\theta_B)$ the undulator was successfully tuned using the Bragg angle as the single parameter. If a smoothly varying intensity distribution is needed, one can change the coefficient α.

Figure 3
(*a*) Calculated (open diamonds) and observed (closed diamonds) undulator gap values giving the peak intensity as a function of Bragg angle for the first (L-mode) and third (H-mode) higher harmonic radiation. (*b*) Difference between the calculated and observed gap values.

3. Goniometer system

For anisotropic single crystals, radial distribution functions along a particular direction are obtained by choosing a sample orientation such that the electrical field vector becomes parallel to a crystallographic axis. For high-T_c superconductivity perovskites with an orthorhombic
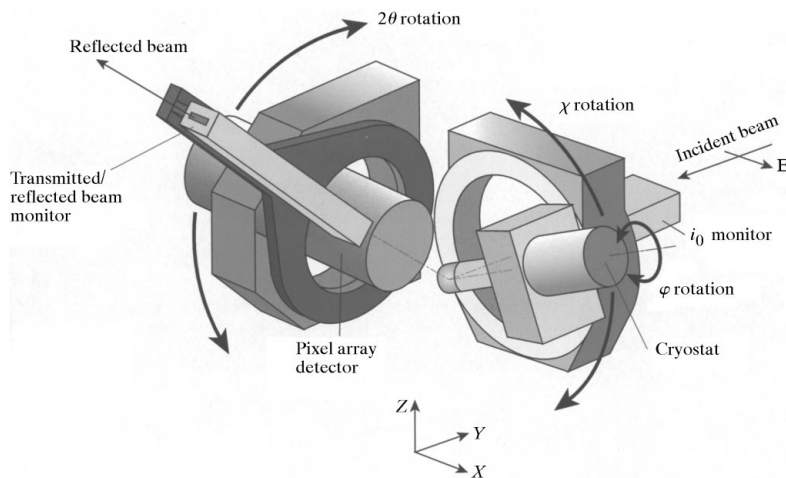

Figure 4
Schematic set-up of the two goniometers. χ and φ rotations in the first goniometer are used to orient a single crystal with respect to the electrical field vector **E**.

symmetry, the electrical field vector should be oriented along the a-, b- or c-axis. In temperature-dependent polarized XAFS experiments a dominant systematic error arises due to the beam inhomogeneity and the uncertainty of a sample geometry and/or beam positions on the sample which defines the probing area. Both geometry and positions should be precisely controlled and kept stable during a scan. In order to meet those requirements a cryostat should have at least φ- and χ-axis rotations and additional translational motions (X and Z) as shown in Fig. 4. Tilting of the sample to set up a grazing-incidence angle is also essential in surface-sensitive XAFS experiments (Oyanagi et al., 1995). In a grazing-incidence geometry, vertical and horizontal sample orientations provide information on the radial distributions parallel and perpendicular to the surface normal, respectively. A grazing-incidence geometry is also useful in pump-and-probe XAFS for minimizing mismatches between X-ray probe and optical pumping (Oyanagi et al., 1998).

Thus we have designed a three-axis goniometer system consisting of two separate goniometers as illustrated in Fig. 4. A sample in a closed-cycle He cryostat mounted on the upstream goniometer (Huber Eulerian cradle 511.1) can be oriented allowing any orientation geometry with respect to the electrical field vector using φ- and χ-axis rotations. The goniometer is useful for temperature-dependent polarized XAFS experiments. An ionization chamber as a transmitted or a reflected beam monitor can be rotated around a 2θ axis of the downstream goniometer (Huber 420). The Ge PAD (Oyanagi, 1998) is mounted

through the base plate of the 2θ goniometer and detects the fluorescence from a sample held in a cryostat. For a horizontal orientation of the cryostat one can also perform X-ray standing wave (XSW) experiments using the same detector for which the reflected beam intensity is monitored by a downstream ion chamber mounted on the 2θ axis. φ, χ and 2θ axes, and Z and X linear motions are remotely controlled. For two polarization geometries ($E \parallel ab$ and $E \parallel c$) for an orthorhombic crystal, a grazing incidence angle δ_0 (usually taken as $1.6°$ to minimize the diffractions) is adjusted by tilting the φ-axis. Fig. 5 shows the front and plan views of the goniometer system.

In structural studies of surfaces and interfaces, XSW experiments provide complementary information with polarized XAFS on the atom positions along the surface normal direction (Zegenhagen, 1993). Once a sample is mounted on the goniometer which allows a conventional two-circle diffractometer geometry, XSW experiments can be performed for the same sample.

4. Detector and electronics

As a high-efficiency X-ray detector, a novel Ge PAD has been developed. The arrangement of 10×10 Ge pixels is illustrated in Fig. 6. In a recent design of a conventional multi-element Ge detector the packing ratio reached 57% (Oyanagi et al., 1998). In a monolithic approach the dead region between pixels can be as small as ~ 0.3 mm which dramatically improves the packing ratio to 80–90%. In this design each pixel (pure Ge) is 10 mm thick and has an effective area of 4.7 mm $\times$ 4.7 mm. The energy resolution is designed to be 190 eV at 5.9 keV at a medium count rate. We estimate the energy resolution at a high count rate (2×10^5 counts s^{-1}) to be ~ 240 eV using a 1 μs peaking time for a commercial digital signal processor.

Each pixel is equipped with a PSC941 preamplifier (Penta FET). Ten field-effect transistor (FET) modules are mounted on a single cooled circuit board and connected to Ge pixels by mechanical contact. All FET circuit boards and preamplifier modules were fabricated and tested. Performance tests for Ge PADs with improved passivated surfaces have shown the high energy resolution (215 eV at
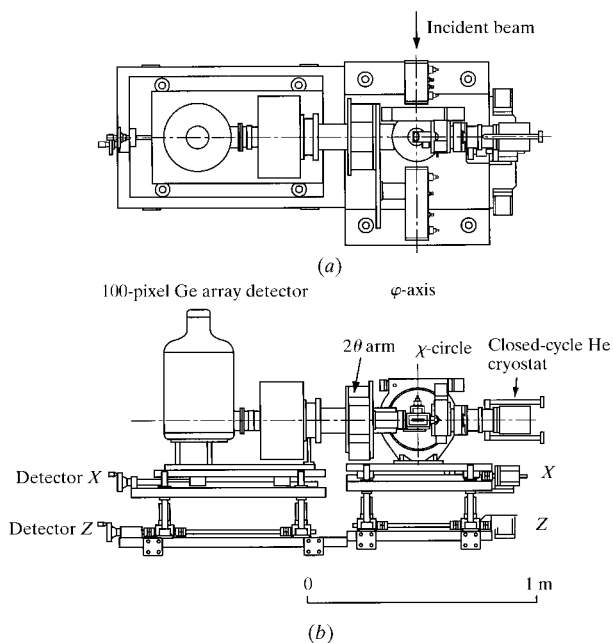

Figure 5
(a) Plan view and (b) front view of a high-brilliance XAFS apparatus installed at BL10XU, SPring-8. Using a χ-circle, a sample on a cryostat can be oriented with either a vertical or horizontal geometry.
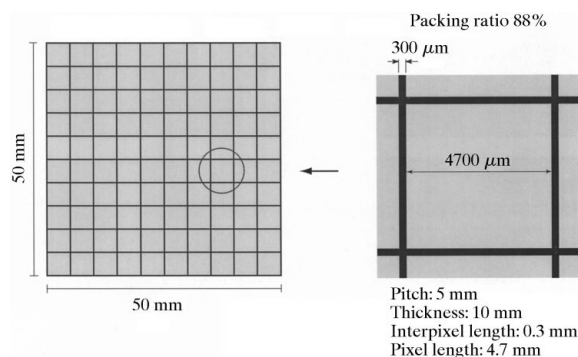

Figure 6
Monolithic Ge pixel array detector.

5.9 keV). In Fig. 7 the energy spectrum for one channel (pixel #85) is shown. Up to now ∼60% of the total 100 pixels are in operation while further research is under way to increase this percentage. Details of the PAD will appear elsewhere (Oyanagi, 2000). In total, a maximum count rate of 2×10^7 counts s^{-1} is expected after the optimization of FET capacitance for high count rate use. For recording a particular fluorescence line, a four-channel digital signal processor (X-ray Instrumentation Association, DXP Model 4 T) is used. For 100 channel outputs, 25 DXP modules are equipped which are controlled *via* a CAMAC interface (WieNer, CC16) and a PC (Dell Computer, Optiplex GXMT5166) running on linux 2.1.30.

5. Performance

Owing to a grazing-incidence angle of $1°$ in an asymmetric double-crystal $(+, -)$ rotated inclined configuration, the power density on the first crystal surface, ∼5 W mm^{-2}, is reduced to 1/57.3. We find that the reflectivity calculated by dynamical theory for an Si(111) reflection becomes larger than the symmetric case by a factor of two; the full width at half-maximum (FWHM) values for rocking curves are 14.9 arcsec at 8 keV for Si(111) and 2.3 arcsec at 24 keV for Si(220). However, the observed energy resolution $\Delta E/E$ given as a convolution of rocking-curve width and an angular divergence multiplied by cot θ_B was less than 2×10^{-4} because of a small angular divergence of the incident beam (4.85 μrad). A mechanical slit placed in front of the monochromator limited the beam to 1 mm.

We evaluated the performance in the low-energy region which is most critical to the quality of the incident beam. Because of a strict limitation on the heat load of the undulator front-end, the minimum gap is limited to 9.6 mm. The lowest energy limit in Bragg angle is $\theta_B = 21.5°$ (5.39 keV) for which the undulator gap value is 9.61 mm. In
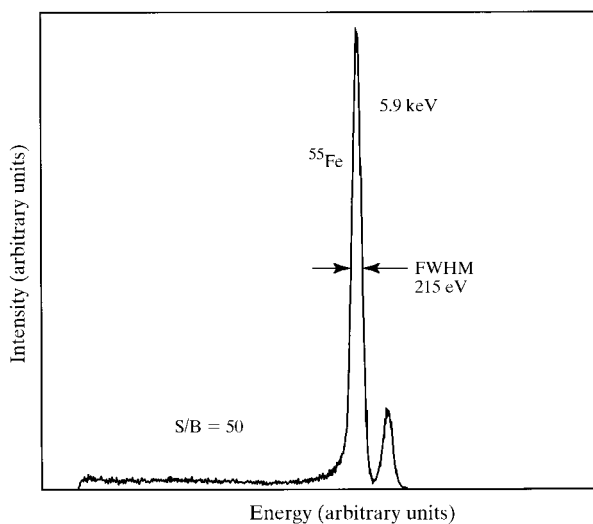
Fig. 8 the Cr K-XANES spectrum for K_2CrO_4 powder is shown. A sharp transition to a bound state (5992.8 eV) demonstrates the high energy resolution of the spectrometer. The evaluation was performed during the initial stage of operation with a ring current of 40–50 mA but it was confirmed that the same performance is available with the present ring current, 70–80 mA. For the Si(111) reflection the higher limit in energy for the H mode ($n = 3$) is 23.1 keV with $\theta_B = 5°$ and a gap value of 12.18 mm. However, since the minimum Bragg angle θ_B of the monochromator is $3°$, the upper limit in energy can be easily extended to 30 keV if the $n = 5$ peak is used (see Fig. 1).

Fig. 9 shows the I_0 intensity variation and Ru K-XAFS spectrum taken for $PrRu_4P_{12}$ powder as a function of

Figure 8
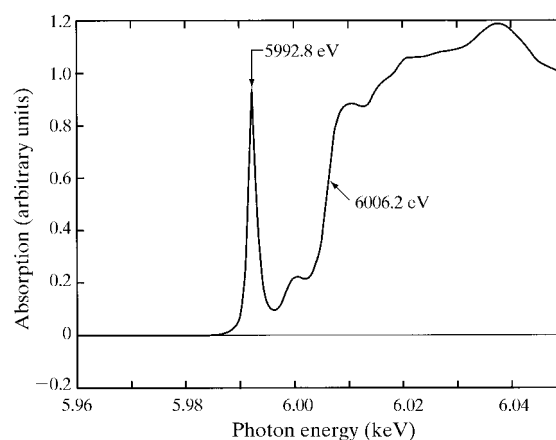Cr K-edge XANES spectrum for K_2CrO_4 powder (Izumi & Nagamori, 1999).

Figure 7
Multichannel analyzer output of pixel #85. S/B = signal-to-background ratio.

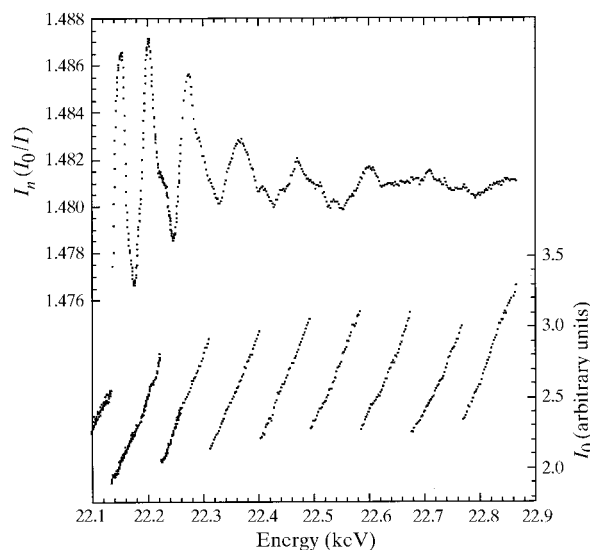**Figure 9**
Expanded Ru K-XAFS spectrum for $PrRu_4P_{12}$ (top) plotted as a function of photon energy (keV) measured in transmission mode (Lee *et al.*, 1999). I_0 intensity variation as undulator and monochromator are scanned from 22.9 keV down to 22.1 keV (bottom).

photon energy (Lee *et al.*, 1999). The saw-tooth shape, *i.e.* gradual decrease of I_0 intensity followed by a sharp increase on decreasing photon energy, is clearly seen. Inspection of the Ru *K*-XAFS spectrum confirmed that there are no glitches related to undulator tuning.

6. Summary

A continuous spectroscopic scan over 1 keV and wide-range tuning over 5–30 keV have been achieved by computer-controlling an undulator gap. For minimizing the tuning time the undulator gap was tuned based on a user-defined criterion. In spite of broadening of the width of the crystal rocking curve due to an asymmetric reflection geometry, a high energy resolution better than 2×10^{-4} at 9 keV was obtained using an Si(111) plane. Two independent high-precision goniometers were combined so that the orientation and position of a sample mounted in a cryostat can be controlled. This allows polarized XAFS including a grazing-incidence experiment in fluorescence mode and XSW experiments. A novel Ge pixel array detector provides a 20 MHz total count rate. The combination of a high-brilliance beam and high-throughput X-ray detector is expected to provide a routine tool for local structures in dilute systems. The performance is demonstrated by high spectral quality (energy resolution, statistics and stability) of XAFS data taken for some powder samples.

ray tracing of the beamline. This work has been performed as the implementation program of the high-brilliance XAFS facility at SPring-8.

References

Argyriou, D. N., Mitchell, J. F., Potter, C. D., Hinks, D. G., Jorgensen, J. D. & Bader, S. D. (1996). *Phys. Rev. Lett.* **76**, 3826–3829.

Bianconi, A., Saini, N. L., Lanzara, A., Missori, M., Rossetti, T., Oyanagi, H., Yamaguchi, H., Oka, T. & Ito, T. (1996). *Phys. Rev. Lett.* **76**, 3412–3415.

Chance, B. (1994). *Synchrotron Radiation in Biosciences*, pp. 247–251. Oxford University Press.

Ishikawa, T. (1995). Unpublished.

Izumi, Y. & Nagamori, H. (1999). Unpublished.

Kitamura, H. (1994). *Rev. Sci. Instrum.* **66**, 2007–2010.

Kolobov, A. V., Oyanagi, H., Tanaka, K. & Tanaka, K. (1997). *Phys. Rev. B*, **55**, 726–734.

Lee, C. H., Oyanagi, H., Sekine, C., Shirotani, I. & Ishii, M. (1999). *Phys. Rev. B*, **60**, 13253–13256.

Oyanagi, H. (1993). *J. Appl. Phys. Suppl.* **32**(2), 861–865.

Oyanagi, H. (1998). *J. Synchrotron Rad.* **5**, 48–53.

Oyanagi, H. (2000). In preparation.

Oyanagi, H., Kolobov, A. V. & Tanaka, K. (1998). *J. Synchrotron Rad.* **5**, 1001–1003.

Oyanagi, H., Saito, M. & Martini, M. (1998). *Nucl. Instrum. Methods*, A**403**, 58–64.

Oyanagi, H., Shioda, R., Kuwahara, Y. & Haga, K. (1995). *J. Synchrotron Rad.* **2**, 99–105.

Rogalev, A., Gotte, V., Goulon, J., Gauthier, C., Chavanne, J. & Elleaume, P. (1998). *J. Synchrotron Rad.* **5**, 989–991.

Sasaki, S. (1994). Private communication.

Uruga, T., Kitamura, H., Kohmura, Y., Kuroda, M., Nagasawa, H., Ohtomo, K., Yamaoka, H., Ishikawa, T., Ueki, T., Iwasaki, H., Hashimoto, S., Kashihara, Y. & Okui, K. (1995). *Rev. Sci. Instrum.* **66**, 2254–2256.

Zegenhagen, J. (1993). *Surf. Sci. Rep.* **18**, 200–271.